

# A Wearable CMOS Biosensor with 3 Designs of Energy-Resolution Scalable Time-Based Resistance to Digital Converter

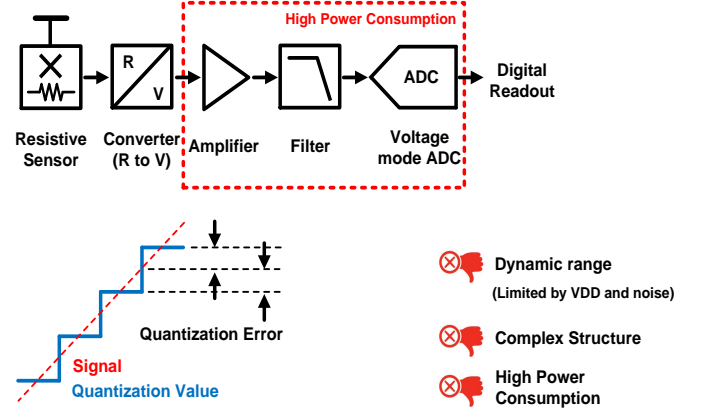
Dong-Hyun Seo, Baibhab Chatterjee, *Student Member, IEEE*, Sean Scott, Daniel Valentino, *Member, IEEE*, Dimitrios Peroulis, *Fellow, IEEE*, and Shreyas Sen, *Senior Member, IEEE*

**Abstract**—This paper presents the design and analysis of a wearable CMOS biosensor with three different designs of energy-resolution scalable time-based resistance to digital converters (RDC), targeted towards either minimizing the energy/conversion step or maximizing bit-resolution. The implemented RDCs consist of a 3-stage differential ring oscillator which is current starved with the resistive sensor, a differential to single ended amplifier, an off-chip counter and serial interface. The first design RDC included the basic structure of time-based RDC and targeted low energy/conversion step. The second design RDC aimed to improve the rms jitter/phase noise of the oscillator with help of speed-up latches, to achieve higher bit-resolution as compared to the first design RDC. The third design RDC reduced the power consumption by scaling the technology with the improved phase-noise design, achieving 1-bit better resolution as that of the second design RDC. Using a time-based implementation, the RDCs exhibit energy-resolution scalability, and consume 861nW with 18-bit resolution in design 1 in TSMC 0.35 $\mu$ m technology. Design 2 and 3 consume 19.1 $\mu$ W with 20-bit resolution using TSMC 0.35 $\mu$ m, and 17.6 $\mu$ W with 20-bit resolutions using TSMC 0.18 $\mu$ m, respectively (both with 10ms read-time, repeated every second). With 30ms read-time, design 3 achieves 21-bit resolution, which is the highest resolution reported for a time-based ADC. The 0.35 $\mu$ m time-based RDC is the lowest-power time-based ADC reported, while the 0.18 $\mu$ m time-based RDC with speed-up latch offers the highest resolution. The active chip-area for all 3-designs are less than 1.1 mm<sup>2</sup>.

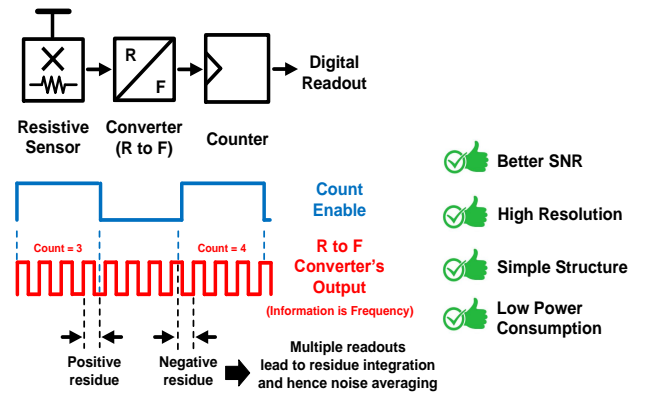
**Index Terms**—CMOS biosensor, wearable device, resistive sensor, resistance to digital converter, time-based ADC, low-power, rms jitter, low phase noise, Energy-resolution scalability, mixed signal circuits.

## I. INTRODUCTION

IN recent years, low-power wearable bio sensing devices have presented great potentials for many biomedical applications including diagnosis, physiological monitoring and health care systems [1]- [5]. The pursuit of convenience for continuous monitoring in both hospital and ambulatory applications requires these devices to have a small form of factor and low power consumption for battery-powered wearable/portable use. Thus, integrated circuits (ICs) are needed in biomedical fields in order to create wearable medical sensing applications. The most critical requirement of medical devices is the accurate transmission of data/information, which requires high bit-resolution. The key challenge in designing high resolution biomedical ICs derives from system/circuit/ambient noise and power, exhibiting trade-offs among achievable resolution, noise and power [6].



(a) Voltage/Current mode Sensor Interfacing Circuit



(a) Time/Frequency mode Sensor Interfacing Circuit

Fig. 1. Inherent advantages provided by time/frequency mode ADCs over voltage/current mode ADCs for low-speed high-resolution resistive sensing applications: (a) traditional voltage/current mode ADC sensor interfacing circuits, (b) time/frequency mode ADC sensor interfacing circuits.

Fig. 1 shows the fundamental advantages provided by time/frequency mode analog-to-digital converter (ADC) over voltage/current mode ADC for low speed and high resolution applications in the noise and supply voltage limited regime. Although digital signal processors and integrated circuits take advantage of technology scaling to achieve improvements in power, speed, size, and cost, scaling of supply voltage cause

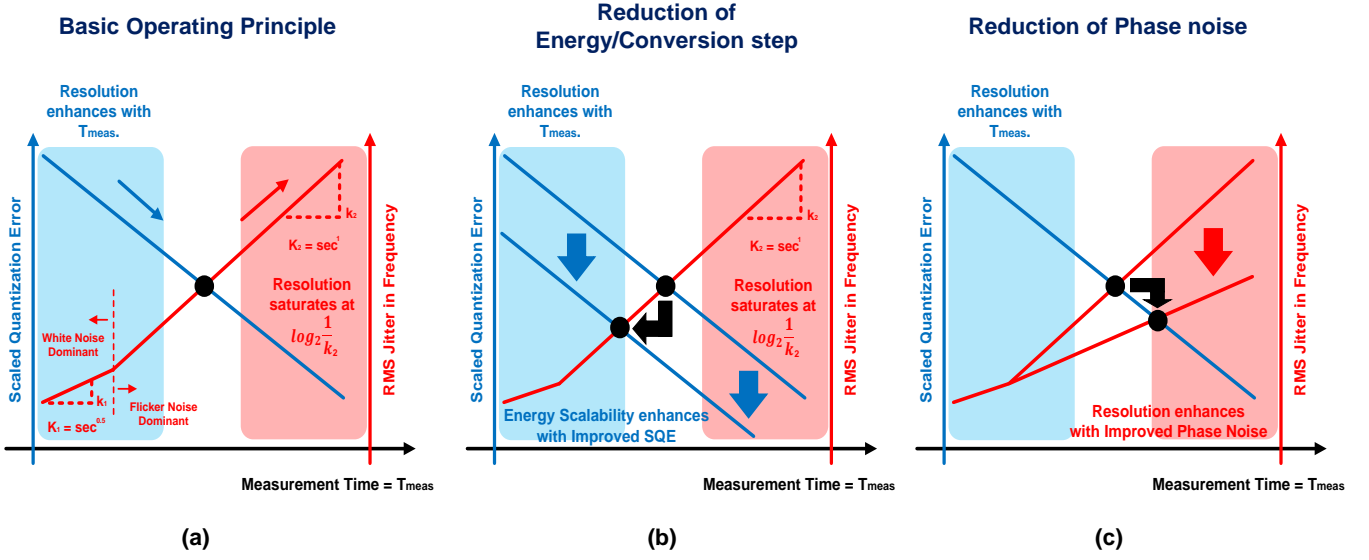


Fig. 2. Operating principle of time-based RDC: (a) resolution trade-offs between scaled quantization noise and jitter/phase noise of the ring oscillator in the design: quantization error decreases with time, whereas jitter accumulates with time, resulting in a saturated maximum achievable resolution in the jitter dominated region (b) reduction in measurement time (and hence measurement energy and energy/conversion step) by reducing the scaled quantization error of the ring oscillator, (c) improvement in resolution resulting from improving jitter/phase noise of the ring oscillator

a significant disadvantage to the available voltage dynamic range. In addition, the voltage/current mode ADC interface requires signal conditioning circuits such as analog amplifiers and filters between the sensor devices and the ADC, making it challenging to reduce power. Also, voltage/current mode ADCs need sophisticated noise cancelling techniques to diminish the quantization noise as displayed in Fig. 1(a), which improves the signal to noise ratio (SNR) and bit-resolution. On the other hand, the reduction of gate delays has led an improvement in "time-resolution" in scaled devices. Furthermore, the time/frequency mode ADC can achieve high resolution with increased enable time which can integrate residues over more time [7]- [8], leading to a time-domain averaging of the noise which is displayed in Fig. 1(b). Thus, sensing the data/information through time-based techniques (which is a time difference between two rising or falling edges) can potentially represent a better solution than sensing in voltage mode (which is a difference between two node voltages), when ADCs are implemented in a scaled process [9]. The time domain ADC can be as simple as a ring oscillator (that converts resistance to frequency by starving the ring oscillator with the resistive sensor), the output frequency of which can be provided to a multi-bit digital counter with a predefined enable time. The output of the counter would be a direct digital representation of the resistance.

Along With the popularization of biomedical applications and their increasing demands, devices with low power consumption and high resolution sensor have been increasingly preferred. Resistive sensors possess numerous strengths, including good stability, low cost, and ease to be interfaced by readout circuits. Due to these strengths, resistive sensors have been extensively practiced and utilized in diverse fields such as physiological monitoring, environmental and biomedical analysis [10]- [13]. As devices that include a resistive sensor

are widely adopted in biomedical applications with diverse dynamic range requirements (such as temperature, pressure, and radiation), this paper aims to analyze energy-resolution scalability of the proposed time-based resistance-to-digital converter (RDC).

In this paper, in order to resolve the challenges and address the aforementioned advantages, the CMOS biosensor is implemented as a resistive sensor and time-based RDC. This paper is organized as follows. Section II describes the operating principle and system architecture of three designs of energy-resolution scalable time-based RDC. Section III presents the details of circuit design with the simulation. Section IV explains and describes the system level simulation and result of time-based RDC. Section V shows experimental results of the implemented chips along with a comparison with the state-of-the-art. Finally, concluding remarks are presented in Section VI.

## II. SYSTEM ARCHITECTURE

Fig. 2 shows the operating principle of CMOS biosensor with time-based architectures that help to achieve better bit-resolution with more measurement time ( $T_{meas.}$ ). The bit-resolution of the time-based RDC is determined by the scaled quantization error (which is the ratio of one counting cycle with the total measurement time, i.e.  $\frac{T}{T_{meas.}}$ ) and the accumulated jitter around desired frequency measured as described in Fig. 2(a). The scaled quantization error (SQE) decreases with an increase in the ( $T_{meas.}$ ), where T refers to a time-period of oscillator. On the contrary, the accumulated rms jitter/phase noise of the ring oscillator linearly increases with  $T_{meas.}$  When the overall phase noise is dominated by the flicker noise of the tail current sources which slowly change, the cycles of oscillation of oscillator constantly change, either accelerating or decelerating, due to the correlated supply and

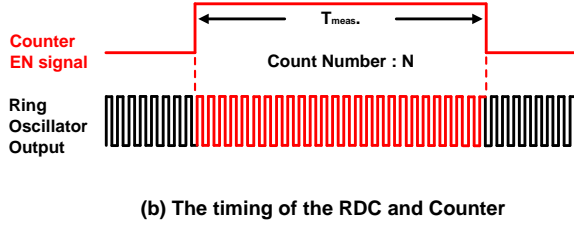
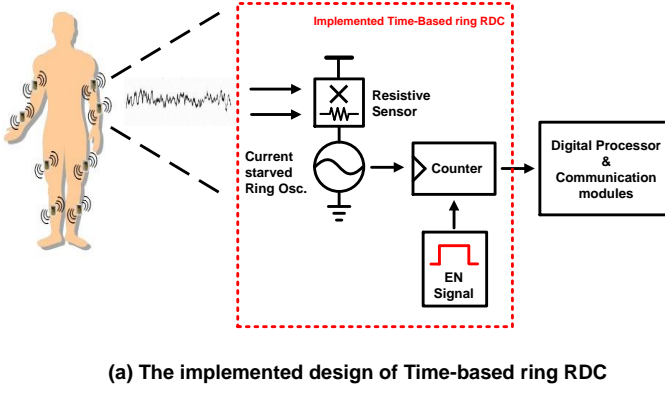


Fig. 3. System architecture: (a) Simplified diagram of time based Ring-RDC based biosensor node, (b) the timing of the RDC and counter

substrate noise. It ends up accumulating a large difference in phase. The correlated nature of noise generates the increased difference quadratically with the total time of accumulation. This results in a rms jitter proportional to the  $T_{meas.}$  [14]- [15]. Combining the effects of SQE with jitter/phase noise, we can write the total scaled quantization error with jitter (SQEJ) as given by Eq. 1.

$$SQEJ = \frac{T + k \times T_{meas.}}{T_{meas.}} \quad (1)$$

where  $k$  refers to the slope of the linearly accumulating rms jitter/phase noise with  $T_{meas.}$ . The bit-resolution can be defined by Eq.2.

$$bit\_resolution = \log_2\left(\frac{1}{SQEJ}\right) \quad (2)$$

Even though  $T_{meas.}$  increases, the bit-resolution is eventually saturated at  $\log_2(\frac{1}{k})$ . There are two ways to enhance the energy-resolution trade-offs in this architecture. One way is to improve the absolute value of the SQE, as shown in Fig 2(b), which results in an unchanged maximum achievable bit-resolution at a lower ( $T_{meas.}$ ), thereby reducing the energy required for measurement as well as the energy per conversion step. The other way is to improve the rms jitter/phase noise as shown in Fig 2(c), which will result in a lower slope and better bit-resolution. In this paper, we focus on the latter way of improving rms jitter/phase noise for increasing the bit-resolution from design 1 to design 2 and 3 of the proposed architecture. The first design provided the basic structure of time-based RDC which aimed at having a low energy consumption [7]- [8]. In the second design, the improved rms jitter/phase noise technique was implemented with the help of speed-up latches. The third design also used the improved rms

jitter/phase noise technique in a scaled technology that offered lower power consumption.

Fig. 3 shows the system architecture. The simplified system architecture of the wearable node, composed of a resistive sensor, a current starved ring oscillator and a digital counter is described in Fig. 3(a). The counter is implemented off-chip. The current starved ring oscillator converts sensor resistance value to oscillation frequency of current starved ring oscillator as a clock output. The clock is supplied to the counter. Fig. 3(b) describes the timing of the RDC and counter. During measurement time ( $T_{meas.}$ ), the counter counts the rising edges of output. The counter output represents the integer number of output cycles in one readout period.

### III. CIRCUIT DESIGN

#### A. 0.35 $\mu$ m Time-Based RDC

Fig. 4(a) shows the 0.35 $\mu$ m time-based RDC which includes resistive sensor devices which are integrated in the same chip, a current starved 3-stage differential ring oscillator (DRO) and a differential to single ended amplifier in order to convert the resistance to frequency, which directly depends on the delay introduced by each inverter stage. Limiting the amount of current is a way to control the delay. In this architecture, the resistive sensors are designed in a way that the generated frequency primarily depends on the amount of current allowed by the resistance, and not on other factors such as the load capacitance  $C_L$ . The concepts of Impulse Sensitivity Function (ISF) and Noise Modulating Function (NMF) are critical to understand that the phase noise at a particular offset increases with the number of stages for a DRO with given power dissipation and frequency. Nonetheless, the phase noise for the single ended ring oscillator SRO works in a different way. Different from the phase noise for the DRO, it does not increase with the number of stages. [14]- [15]. In the case of a SRO, the amount of phase noise does not correlate with the number of stages. However, a SRO has an issue in that it is influenced by common mode supply and substrate noise too easily. Nevertheless, a DRO is more robust against common mode supply and substrate noise even in situations where the phase noise increases linearly with number of stages. Due to this feature, a DRO was chosen over a SRO in this paper, and in order to minimize the issues a DRO has with regard to the phase noise, the number of stage was fixed at a minimal required number (3) for implementation of a DRO. Symmetry was considered to be an important factor during layout as it contributes to minimizing the effects of supply and substrate noise. The differential to single ended converter which is connected to the output of the 3-stage DRO does not require voltage gain, since the input of the differential to single ended converter is rail-to-rail. This means that the transconductance ( $g_m$ ) requirement of the differential to single ended converter is small. As a result, the power consumption of the differential to single ended converter is small with extremely relaxed design constraints, which makes the overall design almost digital and scaling friendly. The 0.35 $\mu$ m time-based RDC has the phase noise of -92.5dBc/Hz @ 100kHz offset and oscillation frequency of 83.2 MHz with 94.4 $\mu$ W

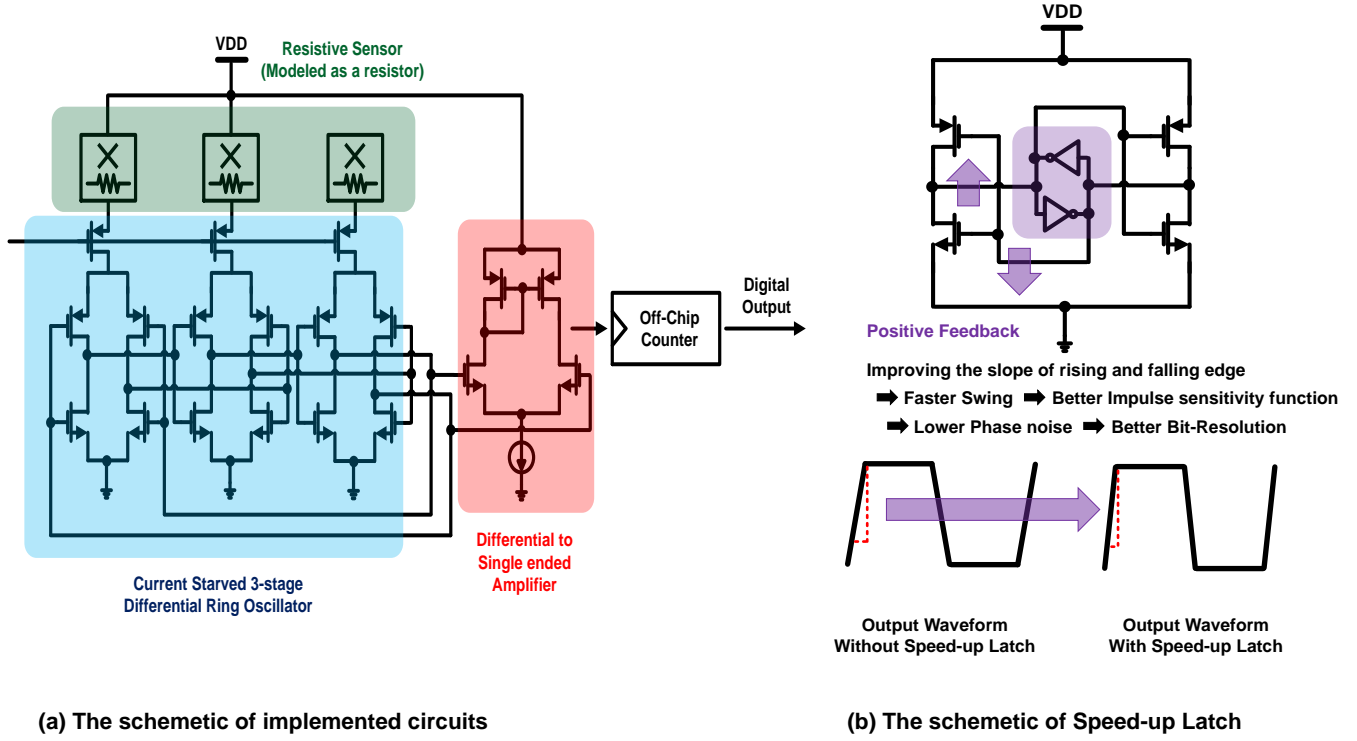


Fig. 4. Implemented circuit schematic: (a) a resistive sensor, a current starved 3-stage differential ring oscillator and a differential to single ended amplifier and (b) improving the slope of rising and falling edge of a 3-stage ring oscillator using speed-up latch.

power consumption (when continuously on) in simulation [7]-[8].

#### B. 0.35 $\mu$ m Time-Based RDC with Speed-up Latch

Fig. 4(b) shows how speed-up latch is implemented with the 0.35 $\mu$ m time-based RDC. The single-side band (SSB) phase noise of the DRO is defined by Eq.3-5 [12].

$$L(\Delta f) = \frac{8}{3\eta} N \frac{kT}{P} \left( \frac{V_{DD}}{V_{Char}} + \frac{V_{DD}}{R_L I_{tail}} \right) \frac{f_o^2}{\Delta f^2} \quad (3)$$

$$V_{Char\_long\_channel} = \frac{\Delta V}{\gamma} \quad (4)$$

$$V_{Char\_short\_channel} = \frac{E_c L}{\gamma} \quad (5)$$

where  $\eta$  is the ratio of stage delay of rising/falling time,  $N$  is the number of DRO stages,  $k$  is the Boltzmann constant,  $T$  is temperature,  $P$  is the power dissipation,  $R_L I_{tail}$  is the output swing,  $f_o$  is the output frequency, and  $\Delta f$  is the offset frequency at which phase noise is calculated. Increasing power reduces phase noise, and reducing frequency of operation will also reduce phase noise at a particular offset. Improving the slope of rising and falling edge of a 3-stage ring oscillator enhances the phase noise performance by improving the swing. Using speed-up latches at the output of each stage of the DRO, we improve the white-noise induced phase noise to -124.5 dBc/Hz @ 1MHz offset, as verified through simulations. The speed-up latch provides positive feedback, improving the slope of rising and falling edge of a 3-stage ring oscillator as shown in Fig. 4(b). In Fig. 5(a), (b) and (c), the simulated

power consumption, frequency and phase noise are presented, respectively, as a function of the sizing of the transistors in the speed-up latch and the DRO. Since the current is limited by the resistive sensor, increasing the size of the DRO transistors capacitively loads the circuit and reduces the frequency. However, since the output of the latch provides positive feedback, the slope of output of each stage of the DRO increases (increasing the swing and frequency) which is described in Fig 5(b). The phase noise improves with the level of power dissipation. However, the best design points are different in terms of power consumption, frequency and phase noise in 0.35 $\mu$ m time-Based RDC with Speed-up Latch. For this reason, a cost function is defined by Eq.6.

$$Cost\_Function = \log_{10} \left( \frac{10^{PN/10}}{F} \times P \right) \quad (6)$$

where  $PN$ ,  $F$  and  $P$  represent the scaled linear phase noise, frequency and power of the DRO, respectively. Reducing this cost function would mean reducing  $PN$  at a high frequency of operation, but at lower power. In Fig. 5(d), the minimized cost function and the optimized sizing of the speed-up latch and sizing of the W/L ratio of the NMOS in the ring oscillator is presented. For the best performance, the NMOS (W/L) ratios of the speed-up latch is determined to be 4 and the NMOS (W/L) ratios of the DRO is determined to be 25 at 83.2 MHz with 1.83 mW power consumption (when continuously on) in simulation.



## 2<sup>nd</sup> Design – 0.35μm Time-Based RDC with Speed-up Latch

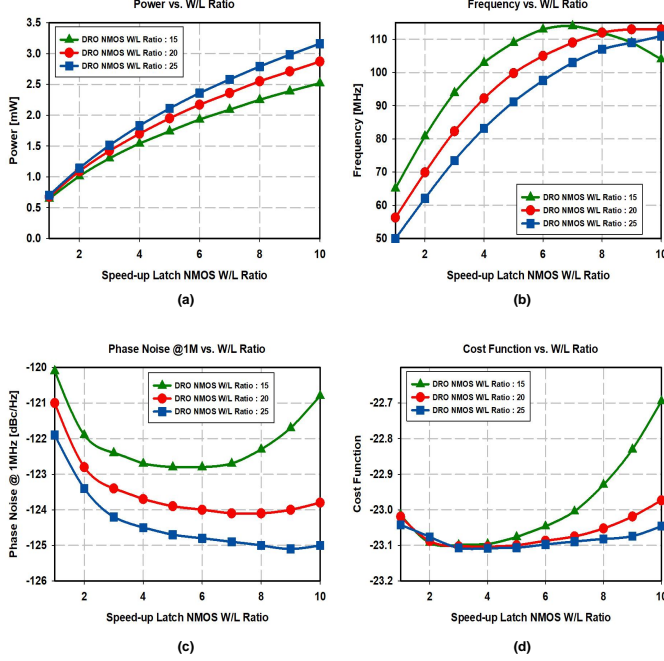


Fig. 5. Simulation results for the time-based RDC in 0.35μm technology: (a) power, (b) frequency, (c) phase noise and (d) minimization cost function vs. sizing of the DRO transistors.

## 3<sup>rd</sup> Design – 0.18μm Time-Based RDC with Speed-up Latch

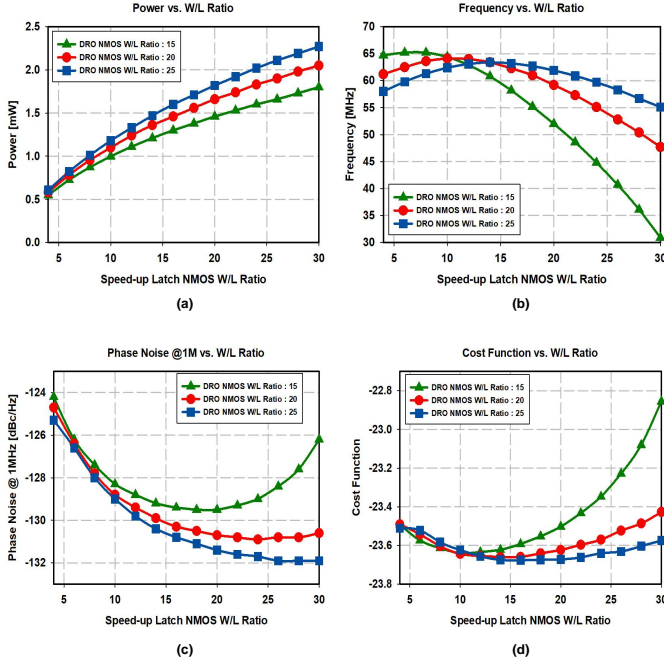


Fig. 6. Simulation results for the time-based RDC in 0.18μm technology: (a) power, (b) frequency, (c) phase noise and (d) minimization cost function vs. sizing of the DRO transistors.

### C. 0.18μm Time-Based RDC with speed-up latch

Technology scaling is the decisive factor that lead to high performance circuit. Threshold voltage of the device must be

## Oscillation Frequency as a function of Sensor Resistor

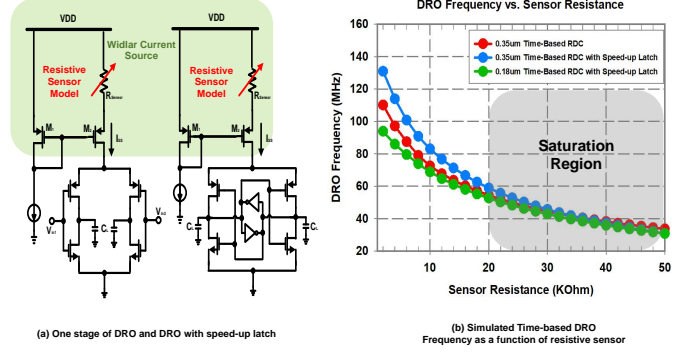


Fig. 7. Simulation results for the time-based RDC in 0.18μm technology: (a) one stage of the DRO and DRO with speed-up latch for analysis of  $R_{sensor}$  range and circuit design and (b) DRO frequency as a function of  $R_{sensor}$ .

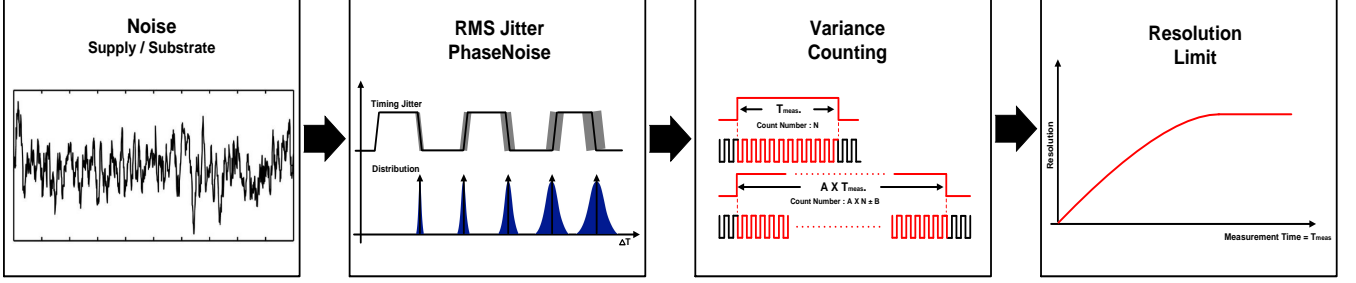
reduced proportionally as supply voltage reduces to sustain the output performance of transistor. Technology scaling has also reduced the gate delay, the parasitic capacitances, and the energy and active power per transition. From the Eq.(3), Improving the delay of a 3-stage ring oscillator enhances the phase noise performance by improving the ratio of stage delay of rising/falling time. Scaling down from 0.35μm to 0.18μm technology with the use of speed-up latches at the output of each stage of the DRO improves the power dissipation and the phase noise to 1.3mW (when continuously on) and -130.5 dBc/Hz @ 1MHz offset, respectively, as verified through simulations. In Fig. 6(a), (b) and (c), the simulated power consumption, frequency and phase noise are presented. More specifically, Fig. 6(a), (b), and (c) show how the simulated power consumption, frequency, and phase noise change according to the size of the transistor in the speed-up latch and the DRO in 0.18μm. Compared to 0.35μm time-based DRO with speed-up latch, power dissipation and phase noise are improved, which accordingly improved the cost function. In Fig. 6(d), the minimized cost function and the optimized sizing of the speed-up latch and sizing of the W/L ratio of the NMOS in the ring oscillator is presented. For the best performance, the NMOS (W/L) ratios of the speed-up latch is determined to be 16 and the NMOS (W/L) ratios of the DRO is determined to be 25 at 61.3 MHz with 1.3 mW (when continuously on) power consumption in simulation.

### D. Resistive Sensor of the Time-Based RDC

A RDC measures the resistance value of a resistive sensor and the input range is a relevant parameter for a RDC. For determining the range of the sensing resistance, the Widlar current source configuration employed in the proposed design was analyzed. Fig. 7(a) shows the widlar configuration. The output current ( $I_{SS}$ ) in saturation region is defined by Eq. 7 [16].

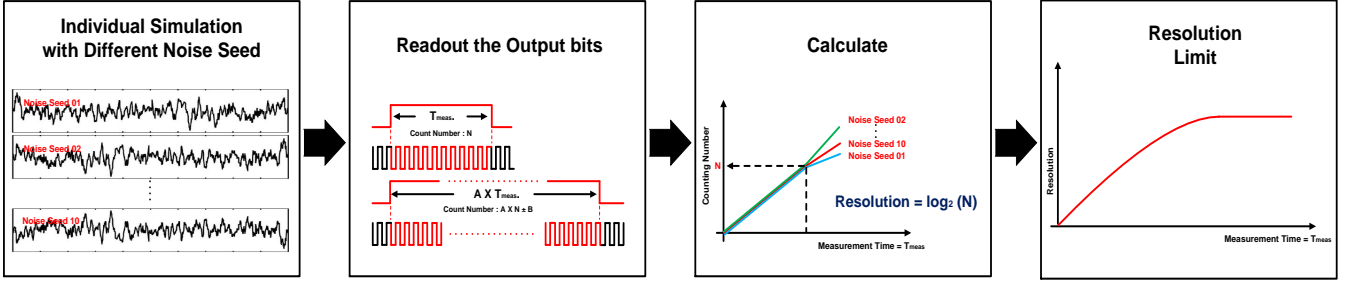
$$I_{SS} = \left( \frac{\sqrt{\frac{2}{\beta_{M2}} + 4R_{sensor}(V_{SG,M1} - |V_{Tp,M1}|)} - \sqrt{\frac{2}{\beta_{M2}}}}{2R_{sensor}} \right)^2 \quad (7)$$

## Physics



(a) Physical Principle of the Resolution Limit

## Simulation Process



(b) Simulation Process of the Resolution Limit

Fig. 8. System level simulation steps for the time-based RDC: (a) physical principle of the resolution limit and (b) simulation process to get the maximum bit-resolution.

$I_{SS}$  is controlled by the resistive sensor ( $R_{sensor}$ ), and oscillation frequency (which is a function of the delay of the ring oscillator stage, and hence a function of the current through the stage) becomes a function of  $R_{sensor}$ . Fig. 7(b) shows the DRO oscillation frequency of the  $0.35\mu\text{m}$  time-based RDC (design 1), the  $0.35\mu\text{m}$  time-based RDC with speed-up latch (design 2) and the  $0.18\mu\text{m}$  time-based RDC with speed-up latch (design 3) respectively, as a function of  $R_{sensor}$ . The oscillation frequency of DRO is saturated beyond around  $20\text{k}\Omega$  in all three cases. Therefore, the input range of the RDCs are  $< 20\text{k}\Omega$ .

In this architecture, the resistive sensors are designed in a way that the generated frequency primarily depends on the amount of current allowed by the resistance. When the values of the three resistive sensors are the same ( $R$ : fully matched scenario), the oscillation frequency would be  $f_{osc} = \frac{1}{2Nt_p}$ , where  $N$  is the number of stages and  $t_p$  is the stage delay corresponding to  $R$ . On the other hand, when the values of the three resistive sensor are not the equal ( $R_1 \neq R_2 \neq R_3$ ), the oscillation frequency would be  $f_{osc} = \frac{1}{2(t_{p1} + t_{p2} + t_{p3})}$  where  $t_{pi}$  is the  $i$ -th stage delay corresponding to  $R_i$ . This means that the final frequency is a function of the average resistance. Due to a delta amount of change in the resistance of the sensor, DRO delay of each stage would be determined by  $R_1 + \Delta R_1$ ,  $R_2 + \Delta R_2$ , and  $R_3 + \Delta R_3$ . The final output frequency can be expressed  $f_{osc} = \frac{1}{2\{(t_{p1} + \Delta t_{p1}) + (t_{p2} + \Delta t_{p2}) + (t_{p3} + \Delta t_{p3})\}}$ , which is again the average of each delay. Given that the resistances of all three sensors increase (or decrease) simultaneously, it is not necessary to have matching as a requirement.

## IV. SYSTEM LEVEL SIMULATION

Fig. 8 describes physics of the resolution limit and the corresponding simulation process. Many noise factors influence the rms jitter of this system. For example, the rms jitter of the system is all affected by flicker noise up conversion in the tail current source and flicker noise from the correlated supply and substrate noise. The rms jitter accumulate linearly with the measurement time ( $T_{meas.}$ ). The linear increase in the rms jitter was theoretically shown in [14] - [15]. However, importantly, the counting number of the rising edges of output does not linearly increase, even if the ( $T_{meas.}$ ) increases, primarily due to rms jitter, which is caused by noise. This subsequently explains the resolution limit of the system, as shown in Fig. 8(a). Fig 8(b) describes the simulation process to demonstrate the limit of the bit-resolution. Simulations are computed and verified via *Spectre<sup>TM</sup>* simulations using TSMC  $0.35\mu\text{m}$  and  $0.18\mu\text{m}$  technology. 10 individual transient simulation were performed with different noise seeds. The result of simulations, which refers to the rising edges of the output bits, is read at specific times. The counting numbers, represented by the 10 separate simulation results along with a different noise seed, are compared at specific times, respectively. The maximum bit-resolution can be obtained from the point where the fluctuation of the counting numbers compared becomes severe.

Fig. 9, Fig. 10 and Fig. 11 each shows the system level simulation result of the  $0.35\mu\text{m}$  time-based RDC (design 1), the  $0.35\mu\text{m}$  time-based RDC with speed-up latch (design 2) and the  $0.18\mu\text{m}$  time-based RDC with speed-up latch (design 3) respectively. Fig. 9(a), Fig. 10(a) and Fig. 11(a) show that the

### 1<sup>st</sup> Design – 0.35 $\mu$ m Time-Based RDC

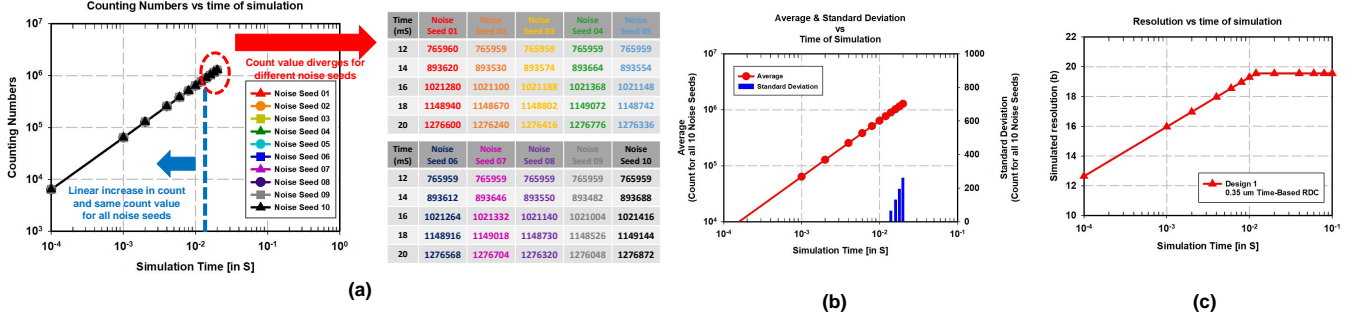


Fig. 9. System level Simulation results for the time-based RDC in 0.35 $\mu$ m technology: (a) 10 individual counting number obtained from the rising edges of output, (b) average and standard deviation of counting numbers for all 10 noise seeds and (c) resolution vs. time of simulation of the 0.35 $\mu$ m time-based RDC (design 1).

### 2<sup>nd</sup> Design – 0.35 $\mu$ m Time-Based RDC with Speed-up Latch

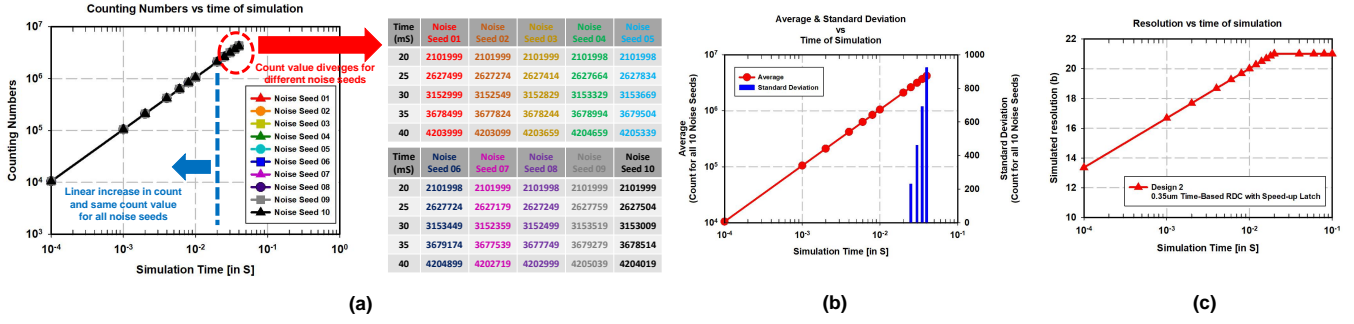


Fig. 10. System level Simulation results for the time-based RDC with speed-up latch in 0.35 $\mu$ m technology: (a) 10 individual counting number obtained from the rising edges of output, (b) average and standard deviation of counting numbers for all 10 noise seeds and (c) resolution vs. time of simulation of the 0.35 $\mu$ m time-based RDC with speed-up latch (design 2).

### 3<sup>rd</sup> Design – 0.18 $\mu$ m Time-Based RDC with Speed-up Latch

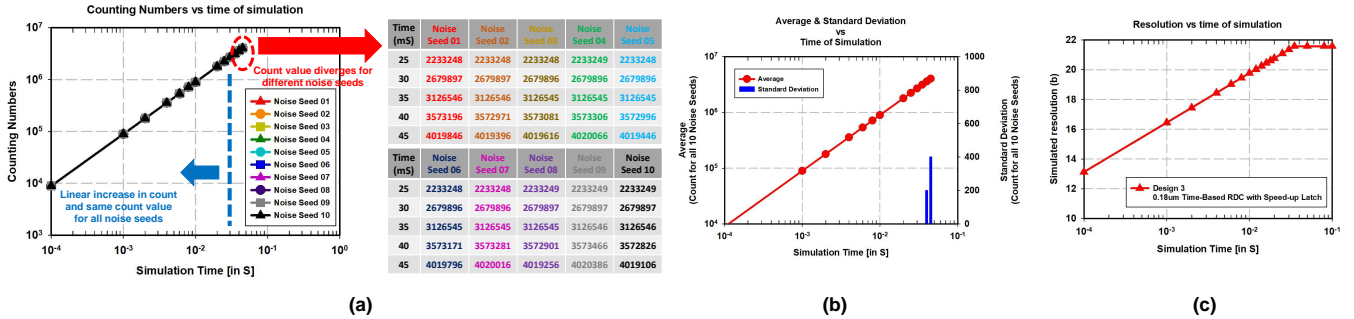


Fig. 11. System level Simulation results for the time-based RDC with speed-up latch in 0.18 $\mu$ m technology: (a) 10 individual counting number obtained from the rising edges of output, (b) average and standard deviation of counting numbers for all 10 noise seeds and (c) resolution vs. time of simulation of the 0.18 $\mu$ m time-based RDC with speed-up latch (design 3).

counting number, which can be obtained from the rising edges of output, increases with the simulation time. The counting number linearly increases and same count value for all noise seeds with the simulation time until it reaches at a certain simulation time, 12ms, 20ms and 35ms, respectively. However, beyond that simulation time, the count value diverges for different noise seeds; rather, it changes randomly in all three

cases. This happens for two reasons. One is that 10 different noise seeds were implemented to each individual simulation. The other is that the oscillation frequency of this system constantly changes, either accelerating or deceleration, due to noise. In order to show the result of simulation, both the average and standard deviation of the counting number, which derived from 10 individual transient simulation performed with

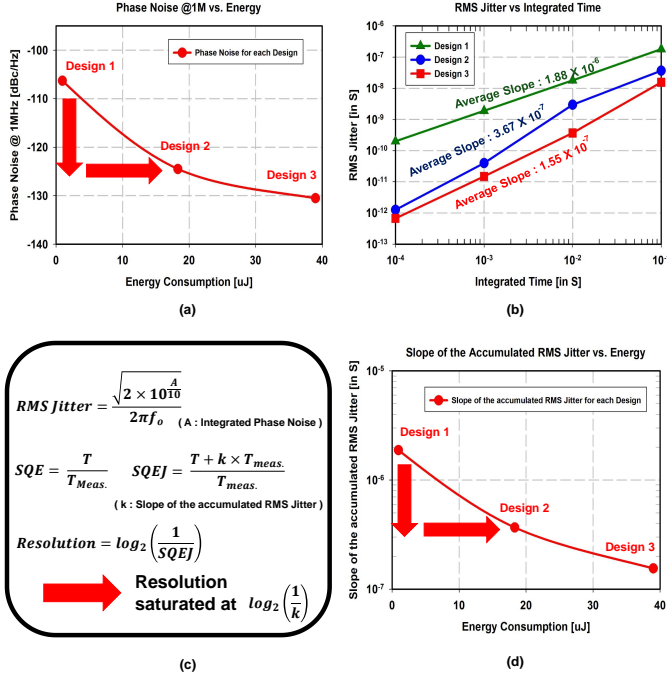


Fig. 12. Simulation results for the three time-based RDC: (a) phase noise vs. energy consumption, (b) the accumulated rms jitter vs. time of measurement, (c) equations and (d) the slope of the accumulated rms jitter vs. energy consumption.

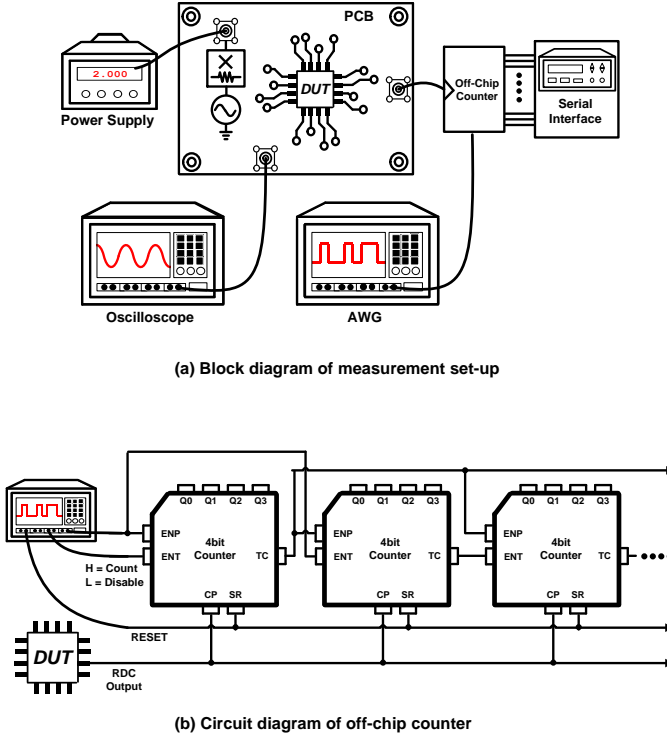


Fig. 13. (a) Block diagram of measurement set-up and (b) circuit diagram of off-chip counter

different noise seeds, were calculated as shown in Fig 9(b), Fig 10(b) and Fig. 11(b). Up until the specific simulation time of 12ms, 20ms and 35ms, the standard deviation for the counting number is zero. However, beyond that simulation time, the

standard deviation increases as the simulation time increases in all three cases. The bit-resolution of the three designs of time-based RDC is plotted against the time of simulation in Fig. 9(c), Fig. 10(c) and Fig. 11(c), respectively. The results show a linear increase in resolution with simulation time on log scale until they saturate in all three cases. The maximum bit resolution can be calculated using Eq.8

$$bit\_resolution = \log_2(N) \quad (8)$$

where N refers to the maximum counting number of the rising edges of output before it significantly changes. This simulation show that the maximum counting number of the rising edges of output for the design1, the design 2 and the design 3 is 765,959, 2,101,999 and 3,126,546 respectively. As a result, the maximum bit-resolution of the design1 and the design 2 and the design3 can be achieved 19.54 bits with 12ms, 21 bits with 20ms, and 21.55 bits with 35ms, respectively. To check the sensitivity of the DRC with respect to voltage and temperature, 10 individual transient simulation were performed with different noise seeds and different supply voltage and temperature. Supply voltage is changing 1.5V-2V and temperature is changing  $-25^{\circ}\text{C}$  to  $100^{\circ}\text{C}$ . The worst case variations with in 17.2 to 19.3 bits in design1, 19.5 to 21.4 bits in design2, and 20.2 to 21.9 bits in design3.

Fig. 12(a) shows the simulation results for the relationship between phase noise and energy consumption of the three designs. The phase noise from design 1 to design 3 is improved even though, energy consumption increased significantly. Based on this phase noise simulation results, the accumulated RMS jitter for integrated time can be calculated. The RMS jitter is calculated using Eq.9

$$RMSJitter = \frac{\sqrt{2 \cdot 10^{A/10}}}{2 \cdot \pi \cdot f_o} \quad (9)$$

where A refers to the integrated phase noise power, and  $f_o$  is the oscillation frequency. Fig. 12(b) plots the accumulated RMS jitter over the integrated time. The maximum achievable resolution can be calculated from the slope of the accumulated RMS jitter. The value of slope for the design 1, the design 2 and the design 3 is  $1.88 \times 10^{-6}$ ,  $3.67 \times 10^{-7}$  and  $1.55 \times 10^{-7}$  respectively. For calculating the average slope, two points at 0.1ms and 10ms are considered. Even though integrated time increases, the bit-resolution is eventually saturated at  $\log_2\left(\frac{1}{k}\right)$  as shown in Fig. 12(c). Fig. 12(d) presents the relationship between the slope of the accumulated RMS jitter and energy consumption of the three designs. Although the energy consumption is increasing gradually, the decrease in the slope of the accumulated RMS jitter dose not keep up with it and is gradually saturated. Our application, we have put priority on resolution even at the expense of energy consumption and hence we are exploring how high can we go in resolution. From the system simulation results, The  $0.35\mu\text{m}$  time-based RDC targeted towards maximizing the energy/conversion step, while the  $0.18\mu\text{m}$  time-based RDC with speed-up latch targeted the highest resolution.



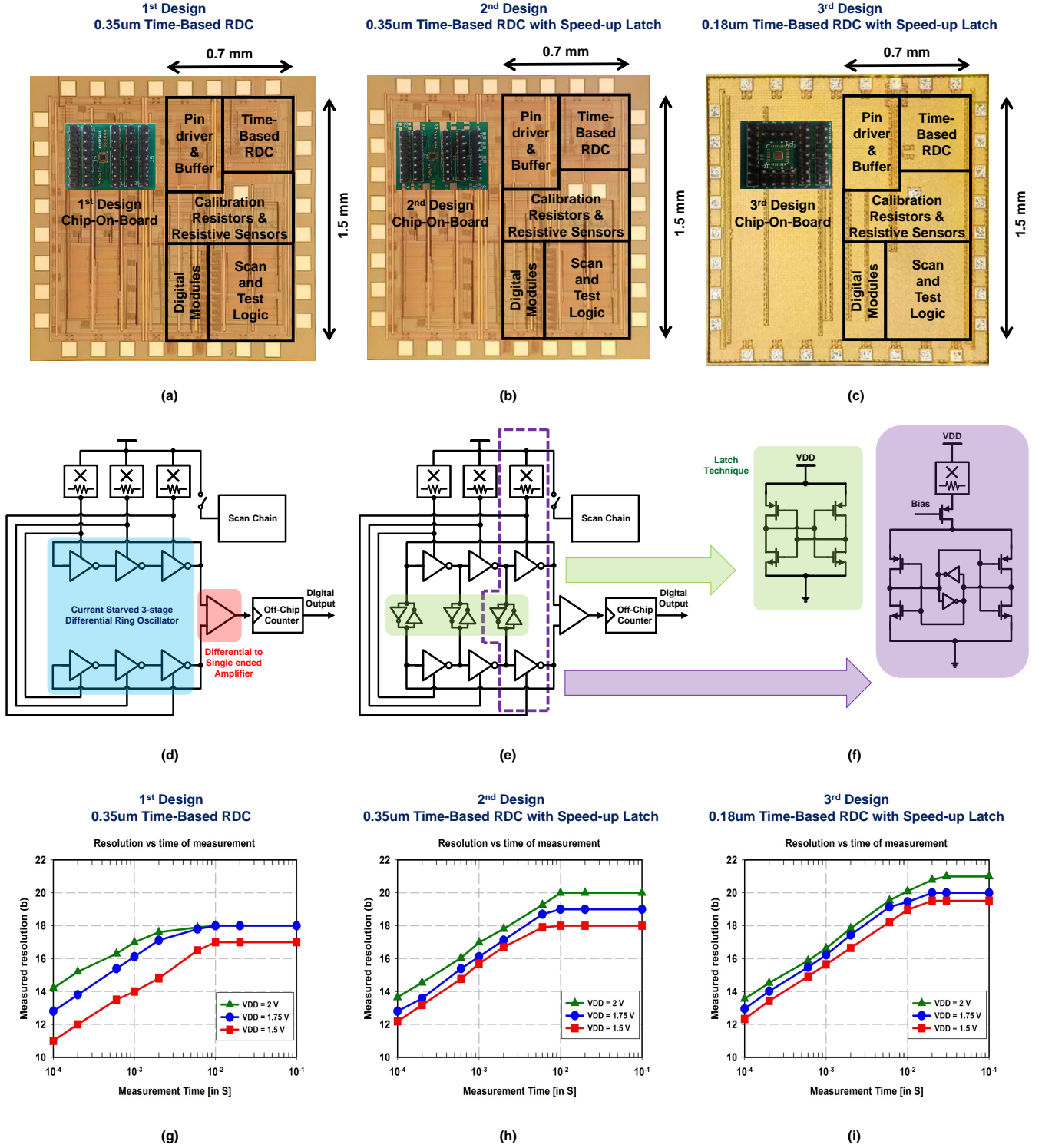


Fig. 14. (a) Chip micrograph of the 0.35 $\mu$ m time-based RDC (design 1), (b) chip micrograph of the 0.35 $\mu$ m time-based RDC with speed-up latch (design 2), (c) chip micrograph of the 0.18 $\mu$ m time-based RDC with speed-up latch (design 3), (d) circuit diagram of 0.35 $\mu$ m time-based RDC, (e) circuit diagram of the 0.35 $\mu$ m and 0.18 $\mu$ m time-based RDC with speed-up latch, (f) detailed circuit schematic consisting of the speed-up latch technique, (g) resolution vs. time of measurement of the 0.35 $\mu$ m time-based RDC (design 1), (h) resolution vs. time of measurement of the 0.35 $\mu$ m time-based RDC with speed-up latch (design 2), and (i) resolution vs. time of measurement of the 0.18 $\mu$ m time-based RDC with speed-up latch (design 3).

## V. SYSTEM LEVEL MEASUREMENT RESULTS

Fig. 13(a) describes the block diagram of measurement setup with 3 designs of energy-resolution scalable time-based RDC. The implemented time-based RDC chip was measured

by using chip-on-board (COB) setup on a customized Printed Circuit Board (PCB) with wire-bonding. The output of the time-based RDC is connected with an off-chip counter. The off-chip counter is implemented with 6 synchronous 4bit

binary counters, which are connected in cascade. The synchronous 4 bit binary counter is manufactured by Texas Instruments, with the device model is named as "CYFCT163T". The "CYFCT163T" device has two types of count enable (CET and CEP) inputs, a terminal count(TC) output for versatility in forming synchronous multistaged counter, and synchronous reset(SR) input. Fig. 13(b) shows the circuit diagram of off-chip counter. This diagram demonstrates how the counter can be used to implement a high-speed N-bit counter. To avoid reducing maximum clocking rate by adding additional stages due to the propagation delay of the terminal out, the output-look-ahead circuit structure is implemented. When additional stages are added the maximum clock frequency of the counter,  $CLK_{MAX}$  remains unchanged. The  $CLK_{MAX}$  is defined by Eq.10.

$$CLK_{MAX} = \frac{1}{TCt_{PHL}} + CEPt_{su} \quad (10)$$

where  $t_{PLH}$  is the propagation delay time, low to high level output, and  $t_{su}$  is the setup time. The output bit of each 4-bit binary counter is connected with serial interface (National Instrument). The generated frequency from the RDC provides the clock signal of the off-chip counter. During measurement time  $T_{meas.}$ , the counter counts the rising edges of output. The counter output represents the integer number of output cycles during one readout within the predefined measurement time  $T_{meas.}$ . The measurement time signal is generated from a RIGOL DG4200 Arbitrary Waveform Generator (AWG). Alternatively, a serial interface with a microcontroller could be utilized for the readout.

Fig. 14(a), (b) and (c) show micro-photograph and Chip-on-board (COB) of the implemented  $0.35\mu\text{m}$  time-based RDC (design 1),  $0.35\mu\text{m}$  time-based RDC with speed-up latch (design 2), and the  $0.18\mu\text{m}$  time-based RDC with speed-up latch (design 3). The active area of the chip of all 3 design is less than  $1.1\text{ mm}^2$  excluding pads. Fig. 14(d) and (e) present the implemented circuit diagram of each time-based RDC. Fig. 14(f) describes the detailed circuit schematic that consists of the speed-up latch technique. The speed-up latch improve the slope of rising and falling edge of a 3-stage ring oscillator and as a result, enhances the phase noise performance by improving the swing. The bit-resolution of the three designs of time-based RDC is plotted against the time of measurement in Fig 14(g), (h) and (i), respectively. The results show a linear increase in resolution with measurement time on log scale for 3 supply voltages until they saturate as a result of jitter/phase noise accumulation, as explained in [7]- [8]. The  $0.35\mu\text{m}$  time-based RDC with speed-up latch (design 2) increases the slope of the rising and falling edges by providing a positive feedback of the output of the latch. Compared to  $0.35\mu\text{m}$  time-based RDC (design 1), the phase noise is improved which subsequently results in higher bit-resolution. The  $0.18\mu\text{m}$  time-based RDC with speed-up latch (design 3) reduces the power consumption for similar readout time. As compared to design 2, 1-bit better resolution can be achieved when readout time is increased to 30ms. The three designs of energy-resolution scalable time-based RDC achieve 18 bit-resolution at  $861\text{nW}$  [7]- [8], 20 bit-resolution at  $19.1\mu\text{W}$  and 21 bit-resolution at  $52.8\mu\text{W}$ , respectively (design 1-2 with

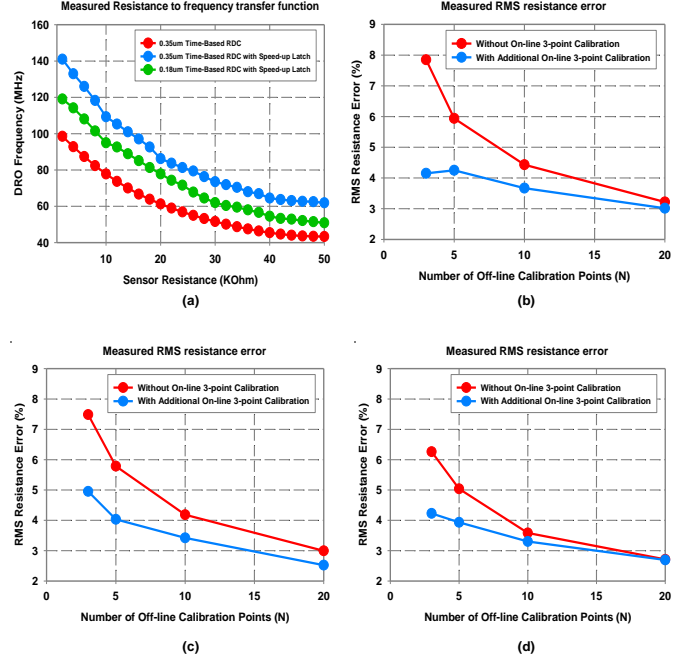


Fig. 15. (a) Measured resistance to frequency transfer function of the 3 RDC designs, (b) measured RMS resistance error (%) for Per-device Off-line calibration, followed by On-line 3-point calibration for the  $0.35\mu\text{m}$  time-based RDC(design 1), (c) measured RMS resistance error (%) for Per-device Off-line calibration, followed by On-line 3-point calibration for the  $0.35\mu\text{m}$  time-based RDC with speed-up latch(design 2) and (d) measured RMS resistance error (%) for Per-device Off-line calibration, followed by On-line 3-point calibration for the  $0.18\mu\text{m}$  time-based RDC with speed-up latch(design 3)

10ms readout time, and design 3 with 30ms readout time, with one readout every second).

The fundamental nature of the resistance to frequency transfer function is non-linear as shown in [8], and the measured result for this transfer function for the 3 designs is shown in Fig. 15(a). This non-linearity arises from the ring-oscillator stage in the Widlar current source configuration which is utilized to convert the degeneration resistance to a corresponding delay and hence to the frequency of the ring oscillator. Because the input signal is of very low frequency (or effectively almost a DC quantity as shown in the application of [8]), the dynamic range can be found from the range of the frequencies (or range of count values from the RDC). This range is found to be about 103dB for the original  $0.35\mu\text{m}$  time-based RDC(design1) [8], 113.5dB for the  $0.35\mu\text{m}$  time-based RDC with the speed-up latch(design2), and 121.1dB for the  $0.18\mu\text{m}$  time-based RDC with the speed-up latch(design3). However, because of the non-linear nature of the resistance to frequency transfer function, calibration and post-processing is required for the proposed RDC. Error due to this calibration becomes a dominant factor in the performance and linearity representation. Hence, instead of performing a traditional FFT (or DNL/INL analysis) to represent linearity, we analyze the effect of the non-linearity calibration method on the overall readout error. The calibration/correction for the non-linearity can be done in 3 ways:

#### 1) Per-device Off-line calibration:

This requires finding out the resistance to frequency trans-

TABLE I  
MEASURED PERFORMANCE SUMMARY OF THE 3-DESIGN TIME-BASED RDC AND COMPARISON TABLE

| Parameter              | This Work : 3-design RDC                                 |                                    |                                    | [17]                 | [18]                  | [19]                  | [20]                 | [21]               |
|------------------------|--|------------------------------------|------------------------------------|----------------------|-----------------------|-----------------------|----------------------|--------------------|
|                        | Time-Based RDC   | Time-Based RDC with speed-up latch | Time-Based RDC with speed-up latch | Time-Based ADC       | Time-Based ADC        | SB-PM RCDC            | RDC                  | RDC                |
| Technology             | 0.35 $\mu$ m   | 0.35 $\mu$ m                       | 0.18 $\mu$ m                       | 0.35 $\mu$ m         | 40 nm                 | 0.18 $\mu$ m          | 0.18 $\mu$ m         | 65 nm              |
| Architecture           | Current Starved Ring Oscillator Based                    |                                    |                                    | VCO Based            | VCO Based             | Oscillator Based      | SAR                  | Switched Capacitor |
| Supply Voltage         | 1.75 V   | 2 V                                | 2 V                                | 5V, 1.8 V            | 1.2 V, 0.45 V         | 1 V                   | 1.8 V                | 1 V                |
| Power                  | 86.1 $\mu$ W   | 1.92 mW                            | 1.76 mW                            | 340 $\mu$ W          | 7 $\mu$ W             | 140 $\mu$ W           | 93.2 $\mu$ W         | 12.3 $\mu$ W       |
| Resolution             | 18 bit   | 20 bit                             | 21 bit                             | 12 bit               | 12 bit                | 16.6 bit              | 11.3 bit             | 9 bit              |
| Readout Time           | 10 ms  | 10 ms                              | 30 ms                              | 400 ms               | 0.75 ms               | 2.93 ms               | 0.92 ms              | 0.5 ms             |
| Dynamic Range          | 103.7 dB   | 113.5 dB                           | 121.1 dB                           | 73 dB                | 79 dB                 | N/A                   | N/A                  | N/A                |
| Off-chip Counter Power | N/A  | 240 mW                             | 205 mW                             | N/A                  | N/A                   | N/A                   | N/A                  | N/A                |
| On-chip Counter Power  | 14 $\mu$ W   | 14.3 $\mu$ W                       | 10.1 $\mu$ W                       | N/A                  | N/A                   | N/A                   | N/A                  | N/A                |
| Energy                 | 861 nJ   | 19.2 $\mu$ J                       | 52.8 $\mu$ J                       | 136 $\mu$ J          | 5.263 nJ              | 410 nJ                | 87.744 nJ            | 6.15 nJ            |
| FoM(Energy/cs)         | 3.29 pJ/cs   | 18.3 pJ/cs                         | 25.1 pJ/cs                         | 37250 pJ/cs          | 4.27 pJ/cs            | 4.04 pJ/cs            | 33 pJ/cs             | 12 pJ/cs           |
| Chip Area              | 0.435 mm <sup>2</sup> (RDC), 1.05mm <sup>2</sup> (total) |                                    |                                    | 0.36 mm <sup>2</sup> | 0.135 mm <sup>2</sup> | 0.175 mm <sup>2</sup> | 0.27 mm <sup>2</sup> | N/A                |

fer function for each device during a pre-measurement (off-line) calibration and applying the inverse of that function during measurement to correct for the non-linearity. This method would result in better accuracy as the number of points used for calibration increase. In the limiting case, error will tend to zero (resulting in extremely high linearity) as the number of points approach infinity. However, this incurs high amount of cost in terms of time and available manual resources.

2) 2) *Per-batch Off-line calibration, followed by an On-line calibration:*

This requires finding out the resistance to frequency transfer function off-line, for one device out of a batch of devices, and eventually update the transfer function for each device on-line, during measurement to take care of PVT (process, voltage and temperature) variations. However, results might be largely inaccurate due to small number of on-line data points for calibration and large process variations.

3) 3) *Subset of Per-device Off-line calibration, followed by an On-line calibration:*

As a compromise between methods 1 and 2, we can perform per-device off-line calibration with a reduced number of points (that will lower the test cost) and then perform an on-line update of the transfer function during measurement to take care of the VT (voltage and temperature) variations.

Fig. 15(b), (c) and (d) shows the measured RMS resistance error (%) for Per-device Off-line calibration, followed by On-line 3-point calibration for 3 designs. For calculating the RMS resistance error, 5 frequency points were randomly selected from all frequencies which correspond to resistances within the 2kohm-50kohm range. The inverse of the resistance to frequency transfer function was applied on these frequencies to find out the resistance. This resistance is compared with the original resistance values to find the RMS error (%) for the 5 points. During this process, the points used for calibration and for test was always kept separate. The number of off-line calibration points are varied from 3 to 20, while the number of

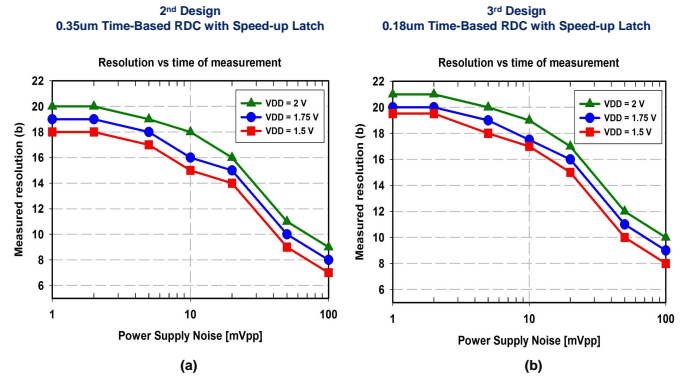


Fig. 16. Resolution vs. supply noise measurement (a) 0.35 $\mu$ m time-based RDC with speed-up latch (design 2), and (b) 0.18 $\mu$ m time-based RDC with speed-up latch (design 3), showing > 18 bit resolution is possible even with 10mV (peak-to-peak) supply noise.

on-line calibration points is set to 3 (which is a feature of all 3 designs, and is shown in detail in [8]). With the additional automatic on-line calibration, the number of points required for off-line calibration reduces for similar amount of rms error.

Table I summarizes the performance of the three designs of energy-resolution scalable time-based RDC in comparison with state-of-the-art high resolution time-based ADC architectures. The 0.35 $\mu$ m time-based RDC consumes the lowest energy, which is 861 nJ with 10 mSec, among all ADCs and the 0.18 $\mu$ m time-based RDC with speed-up latch offers the highest resolution, which is 21 bit with 30 mSec, among all ADCs. From the perspective of the energy/conversion step, 0.35 $\mu$ m time-based RDC shows the best performance which is 3.29 pJ/bit, among all ADCs. The existing time-based approaches utilize over-sampling the input signal for better resolution. However, the proposed approach converts input signal to a corresponding frequency and then measure this frequency over a longer period of time, thereby under-sample it. One primary advantage of under sampling is low power. Additionally, the proposed time based RDC (design 1) has the advantage of energy-resolution scalability – a higher

resolution can be obtained simply by measuring the DRO frequency over longer time, while measurement over a shorter time results in a lower resolution, but with a lower amount of energy. Traditional time-based ADCs would need to change the frequency of the system clock to achieve energy-resolution scalability – thereby adding additional complexity to the system. In conclusion, the basic time-based RDC has the best energy/conversion step and the time-based RDC with speed-up latch improves rms jitter/phase noise to achieve high bit-resolution.

Among the factors that degrade the phase noise performance of oscillators, power supply noise is one of the most dominant in terms of its effect on both the frequency and phase of the oscillator. The power supply voltage affects delay of ring oscillator. In a current starved ring oscillator, power supply noise will reflect as current fluctuations. Fig. 15 shows the bit-resolution of the time-based RDC with respect to the power supply noise amplitude. As the amplitude of the power supply increases, the bit-resolution decreases for all the designs. However, even with 10mV peak-to-peak supply noise, the resolution of the second and third design of RDCs remain > 18-bit, which was the phase-noise limit of design 1. When the sensors are powered from a battery for wearable applications, the effects of supply noise would be much lower.

## VI. CONCLUSION

In this paper, we presented the design and analysis of a wearable CMOS biosensor with 3 designs of energy-resolution scalable time-based resistance to digital converter (RDC). The implemented RDC consisted of a current starved differential ring oscillator, a differential to single ended amplifier, and a off-chip counter in order to convert the change in resistance to equivalent frequency. To the best of the authors' knowledge, the  $0.35\mu\text{m}$  time-based RDC is the lowest-power time-based ADC reported till date, while the  $0.18\mu\text{m}$  time-based RDC with speed-up latch offers the highest resolution. Insights on the energy-resolution trade-offs, scalability aspects and effects of power supply noise are also discussed in the paper. For the low frequency signal, this implemented RDC can detect with high resolution. We wanted to explore the power/performance trade-off in experiment through 3 different design variations, tapeout and IC measurements. As future work, architectures to improve the scaled quantization error would be explored, which would achieve similar resolution with a lower readout time, thereby improving the energy/conversion step.

## REFERENCES

- [1] D. J. Rairigh, G. A. Warnell, C. Xu, E. T. Zellers, and A. J. Mason, "CMOS Baseline tracking and cancellation instrumentation for nanoparticle-coated chemiresistors," *IEEE Trans. Biomed. Circuits Syst.*, vol. 3, no. 5, pp. 267-276, Oct. 2009.
- [2] L. Shu, X. Tao and D. D. Feng, "A new approach for readout of resistive sensor arrays for wearable electronic applications," *IEEE Sensors J.*, vol. 15, no. 1, pp. 442-452, Jan. 2015.
- [3] J. -W. Kwon, D. -H. Jin, H. -J. Kim, S. -I. Hwang, M. -C. Shin, J. -H. Cheon, and S. -T. Ryu, "A low-power TDC-configured logarithmic resistance sensor for MLC PCM readout," *IEEE Sensors J.*, vol. 16, no. 14, pp. 5524-5535, Jul. 2016.
- [4] F. Lorussi, W. Rocchia, E. P. Scilingo, A. Tognetti, and D. De Rossi, "Wearable, redundant fabric-based sensor arrays for reconstruction of body segment posture," *IEEE Sensors J.*, vol. 4, no. 6, pp. 807-818, Jul. 2016.
- [5] M. Tavakoli, L. Turicchia, and R. Sarpeshkar, "an ultra-low-power pulse oximeter implemented with an energy-efficient transimpedance amplifier," *IEEE Trans. Biomed. Circuits Syst.*, vol. 4, no. 1, pp. 27-38, Feb. 2010.
- [6] R. R. Harrison, and C. Charles, "A low-power low-noise CMOS amplifier for neural recording applications," *IEEE J. Solid-States Circuits*, vol. 38, no. 6, pp. 958-965, Jun. 2003.
- [7] B. Chatterjee, C. Mousoulis, S. Maity, A. Kumar, S. Scott, D. Valentino, D. Peroulis, and S. Sen, "A Wearable Real-time CMOS Dosimeter with Integrated Zero-bias Floating-Gate Sensor and an 861nW 18-bit Energy-Resolution Scalable Time-based Radiation to Digital Converter" *2019 IEEE Custom Integrated Circuits Conference (CICC)*, 2019
- [8] B. Chatterjee, C. Mousoulis, D. -H. Seo, S. Maity, A. Kumar, S. Scott, D. Valentino, D. Peroulis, and S. Sen, "A wearable real-time CMOS dosimeter with integrated zero-bias floating gate sensor and an 861nW 18-bit energy-resolution scalable time-based radiation to digital converter" *IEEE J. Solid-States Circuits*, Dec. 2019.
- [9] M. M. Elsayed, V. Dhanasekaran, M. Gambhir, J. Silva-Martinez, and E. SÁnchez-Sinencio, "A 0.8 ps DNL time-to-digital converter with 250 MHz event rate in 65 nm CMOS for time-mode-based  $\Delta\Sigma$  modulator," *IEEE J. Solid-States Circuits*, vol. 46, no. 9, pp. 2084-2098, Sep. 2011.
- [10] J. Lv, H. Zhong, Y. Zhou, B. Liao, J. Wang, and Y. Jiang, "Model-based low-noise readout integrated circuit design for uncooled microbolometers," *IEEE Sensors J.*, vol. 13, no. 4, pp. 1207-1215, Apr. 2013.
- [11] D. J. van den Heever, K. Schreve, and C. Scheffer, "Tactile sensing using force sensing resistors and a super resolution algorithm," *IEEE Sensors J.*, vol. 9, no. 1, pp. 29-35, Jan. 2009.
- [12] R. S. Saxena, N. K. Saini, and R. K. Bhan, "Analysis of crosstalk in networked arrays of resistive sensors," *IEEE Sensors J.*, vol. 11, no. 4, pp. 920-924, Apr. 2011.
- [13] J. W. Gardner, P. K. Guha, F. Udrea, and J. A. Covington, "CMOS interfacing for integrated gas sensors: A review," *IEEE Sensors J.*, vol. 10, no. 12, pp. 1833-1848, Dec. 2010.
- [14] A. Hajimiri, S. Limotyrakis, and T. H. Lee, "Jitter and phase noise in ring oscillators," *IEEE J. Solid-States Circuits*, vol. 34, no. 6, pp. 790-804, Jun. 1999.
- [15] A. Abidi, "Phase noise and jitter in CMOS ring oscillators," *IEEE J. Solid-States Circuits*, vol. 41, no. 8, pp. 1803-1816, Aug. 2006.
- [16] P. Gray, R. Meyer, P. Hurst and S. Lewis, "Analysis and Design of Analog Integrated Circuits." 4th. Ed, NY, USA: John Wiley & Sons, 2001.
- [17] P. Prabha, S. J. Kim, K. Reddy, S. Rao, N. Griesert, A. Rao, G. Winter, and P. K. Hanumolu "A Highly Digital VCO-Based ADC Architecture for Current Sensing Applications," *IEEE J. Solid-States Circuits*, vol. 50, no. 8, pp. 1785-1795, Aug. 2015.
- [18] W. Jiang, V. Hokykyas, H. Chandrakumar, V. Karkare, and D. Markovic, "A  $\pm 50\text{-mV}$  Linear-Input-Range VCO-Based Neural-Recording Front-End With Digital Nonlinearity Correction," *IEEE J. Solid-States Circuits*, vol. 52, no. 1, pp. 173-184, Jan. 2017.
- [19] A. K. George, W. Shim, M. Je, and J. Lee, "A 114-AF RMS-Resolution 46-NF/10-M $\Omega$  -Range Digital-Intensive Reconfigurable RC-to-Digital Converter with Parasitic-Insensitive Femto-Farad Baseline Sensing," *2018 IEEE Symposium on VLSI Circuits*, 2018.
- [20] K. C. Koay and P. K. Chan, "A Low Energy-Noise 65nm CMOS Switched-Capacitor Resistive-Bridge Sensor Interface," *IEEE Transactions on Circuits and Systems I: Regular Papers*, vol. 64, no. 4, pp. 799-810, 2017.
- [21] B. Lee, H. Kim, J. Kim, K. Han, D.-I. D. Cho, and H. Ko, "A low-power 33 pJ/conversion-step 12-bit SAR resistance-to-digital converter for microsensors," *Microsystem Technologies*, vol. 25, no. 5, pp. 2093-2098, 2018.